

Hole-Induced Electronic and Optical Transitions in $\text{La}_{1-x}\text{Sr}_x\text{FeO}_3$ Epitaxial Thin Films

Le Wang¹, Yingge Du^{1*}, Peter V. Sushko¹, Mark E. Bowden², Kelsey A. Stoerzinger¹, Steven M. Heald³, Mark. D. Scafetta¹, Tiffany C. Kaspar¹, Scott. A Chambers^{1*}

¹Physical and Computational Sciences Directorate, Pacific Northwest National Laboratory, Richland, Washington 99354, USA

²Environmental Molecular Sciences Laboratory, Pacific Northwest National Laboratory, Richland, Washington 99352, USA

³Advanced Photon Source, Argonne National Laboratory, Lemont, Illinois 60439, USA

*Authors to whom correspondence should be addressed: yingge.du@pnnl.gov and scott.chambers@pnnl.gov.

We have investigated the electronic and optical properties of epitaxial $\text{La}_{1-x}\text{Sr}_x\text{FeO}_3$ for $0 \leq x \leq 1$ prepared by molecular beam epitaxy. Core-level and valence-band x-ray photoemission features monotonically shift to lower binding energy with increasing x , indicating downward movement of the Fermi level toward the valence band maximum. Combining valence band photoemission and O K -edge x-ray absorption data, we map the evolution of the occupied and unoccupied bands and observe a narrowing of the gap, along with a transfer of state density from just below to just above the Fermi level as a result of hole doping. In-plane transport measurements confirm that the material becomes a p -type semiconductor at lower doping levels and exhibits a conversion from semiconducting to metallic behavior at $x = 1$. Low-energy optical transitions revealed by spectroscopic ellipsometry are explained based on insight from theoretical densities of states and first-principles calculations of optical absorption spectra.

Keywords: Hole doping, Optical absorption, Hybrid functional calculations, Epitaxial oxide films, Molecular beam epitaxy, LaFeO_3 .

I. INTRODUCTION

Perovskite (ABO_3 -type) transition-metal oxides have been of significant interest for several decades because of their intriguing properties. These include metal-insulator transitions (MIT) [1], colossal magnetoresistance (CMR) [2], high-temperature superconductivity [3], and ferroelectricity [4]. These materials have also been of interest for applications in renewable energy technologies including electrochemical and photoelectrochemical water splitting [5-7], photovoltaic solar cells [8,9], and solid oxide fuel cells [10,11]. $LaFeO_3$ (LFO) is a wide-gap ($E_g \sim 2.3$ eV) antiferromagnetic insulator, [12] whereas stoichiometric $SrFeO_3$ (SFO) is a helimagnetic metal [13]. As a result, the $La_{1-x}Sr_xFeO_3$ (LSFO) solid solutions are of interest for solar water splitting because the (in principle) tunable band gap can enhance light absorption across the visible portion of the solar spectrum [14-16]. It has been shown that LFO is orthorhombic at room temperature. However, increasing the Sr concentration alters the crystal structure to rhombohedral near $x = 0.3$ and to cubic near $x = 0.8$ [17,18]. In addition, hole doping by Sr^{2+} substitution for La^{3+} introduces p -type polaron hopping conductivity and enhances the electrocatalytic oxygen evolution reaction (OER) [19,20]. In our previous work, we found that Sr doping lowers the optical bandgap and increases the photovoltage to more than 0.5 V for $La_{0.8}Sr_{0.2}FeO_{3-\delta}$ under 460 nm blue light emitting diode (LED) illumination, in contrast with a negligibly small value for pure LFO [21]. Determining how the electronic and optical properties evolve as a function of Sr content in LSFO is thus critical to understanding and controlling the OER activity in this system.

Assuming no loss of oxygen, Sr^{2+} substitution for La^{3+} should dope holes into the Fe-O hybridized valence band [22,23], resulting in an increase in the nominal Fe valence from 3+ to 4+ [24]. However, LSFO films are often found to be oxygen deficient as the oxygen vacancy (V_O) formation energy is low [25,26], leading to hole compensation, and the Fe valence remains closer to 3+. As shown by Xie *et al.* [26], the electronic structure and transport properties of LSFO films are very sensitive to the oxygen stoichiometry. Post annealing of films grown by molecular beam epitaxy (MBE) to fill as many oxygen vacancies as possible is critical in uncovering the intrinsic properties of LSFO [27]. Wadati *et al.* [28] investigated the electronic structure of LSFO films by X-ray photoemission spectroscopy (XPS) and X-ray absorption spectroscopy (XAS). These authors found that the valence band (VB) spectral feature nearest to Fermi level (E_F) becomes weaker and moves toward E_F as x was increased. However, the

maximum x value they investigated was 0.67. She *et al.* [20] reported Fe $2p$ spectra for LSFO ($0 \leq x \leq 1$) power samples, but the binding energy scale was not calibrated and the VBs were not directly measured. Scafetta *et al.* [24,29] published a careful investigation of the optical properties of LSFO which revealed that increasing x induces systematic changes in the optical spectra, including a red-shift of the absorption features at energies below the LFO band gap. However, due to the limited photon energy range of the spectroscopic ellipsometer used in those studies ($h\nu = 1.2$ to 5 eV), the onset of the absorption edges could not be seen, which ultimately prevented these authors from accurately estimating band gap energies in their LSFO samples.

In this study, we seek to fill in the gaps in existing knowledge of this system by investigating a set of well-defined, epitaxial $\text{La}_{1-x}\text{Sr}_x\text{FeO}_3$ films over the full range of x , combining x-ray photoemission and absorption spectroscopies with first-principles theory, and using spectroscopic ellipsometry from the infra-red to the ultraviolet to accurately map and understand the origin of the densities of states. All films were grown on (001)-oriented SrTiO_3 (STO) substrates by oxygen plasma assisted molecular beam epitaxy (OPA-MBE). Activated oxygen was used to maximize the extent of LSFO film oxidation. By combining *in situ* core-level Fe $2p$ and VB photoemission spectra, *ex situ* Fe and O K -edge x-ray absorption spectra, in-plane electrical transport and optical absorption data, we develop a more complete understanding of the evolution of LSFO functional properties with Sr mole fraction. We also reveal the origins of the low-energy optical absorption bands by carrying out time-dependent density functional theory (TDDFT) simulations.

II. METHODS

Epitaxial $\text{La}_{1-x}\text{Sr}_x\text{FeO}_3$ films with $x = 0, 0.2, 0.37, 0.5, 0.8,$ and 1.0 and thicknesses of 10 - 30 nm were grown on undoped TiO_2 -terminated $\text{SrTiO}_3(001)$ (STO) substrates by OPA-MBE. La, Sr, and Fe were evaporated from high temperature effusion cells. Evaporation rates were calibrated prior to film growth using a quartz crystal oscillator. The substrate temperature was 700°C , and the partial pressure of activated oxygen from an electron cyclotron plasma source in the MBE chamber was $\sim 2 \times 10^{-6}$ Torr. *In situ* reflection high-energy electron diffraction (RHEED) was used to monitor the overall growth rate and surface structure. After film growth, the sample temperature was lowered to ambient at a rate of $30^\circ\text{C}/\text{min}$ in $\sim 2 \times 10^{-6}$ Torr of activated oxygen.

In situ XPS along with *ex situ* AFM measurements were carried out on the as-grown samples. In order to obtain fully oxidized LSFO, the as-grown films were post-annealed by heating to 600°C in activated oxygen at a chamber pressure of $\sim 3 \times 10^{-5}$ Torr for one hour and then cooled to 200°C at a rate of 5°C/min, held at this temperature for two hours, and further cooled at 1°C/min until the heater reached zero output power. The films were kept in the activated oxygen stream at $\sim 3 \times 10^{-5}$ Torr for another hour once reaching room temperature [30].

High-resolution XPS spectra excited with monochromatic Al K_{α} x-rays were measured at normal emission with a Scienta R3000 electron energy analyzer in an appended chamber. The total energy resolution is 0.40 eV. Spectra were measured using an electron flood gun to compensate the positive photoemission charge because not all films were sufficiently conductive, and those that were conductive were not grounded. Samples were measured *in situ* immediately after film deposition, after post-growth annealing in activated oxygen, and a third time after removal from UHV to affix a small polycrystalline Au foil to the corner of each film surface using Cu tape, followed by a 10 min. UV/ozone cleaning on the bench. The Au $4f_{7/2}$ peak was used to calibrate the binding energy scale which is not accurate in an absolute sense because of charging and the use of a flood gun. Some residual contamination remained on the film surfaces after removal from UHV and Au foil attachment, as evidenced by weak features on the higher binding energy side of the O $1s$ lattice peaks, along with very weak C $1s$ peaks. O K -edge near-edge x-ray absorption fine structure (NEXAFS) data were collected in electron yield mode at Beamline 9.3.2 at the Advanced Light Source (ALS) at Lawrence Berkeley National Laboratory. A linear pre-edge background was subtracted from the spectra, followed by normalization to the post-edge and five-point smoothing. The latter did not alter the spectral features in any significant way. Fe K -edge NEXAFS was measured at the Advanced Photon Source at Argonne National Laboratory.

Film crystallography of the annealed films was investigated by high-resolution X-ray diffraction (HRXRD, Philips X'Pert diffractometer) with Cu $K_{\alpha 1}$ radiation ($\lambda = 1.5406 \text{ \AA}$). Spectroscopic ellipsometry (SE) measurements of the annealed films were performed using a rotating analyzer based instrument with a compensator (V-VASE; J.A. Woollam Co., Inc.) over the spectral range from 0.36 to 4.76 eV. Spectra were collected at three different incident angles (65°, 70° and 75°). A simple two-layer model was used to extract the refractive index (n) and

extinction coefficient (k) for each film. The inter-band optical transitions were modelled as direct, dipole-forbidden excitations [12,19]. To this end, the linear regions in the quantities $(\alpha E)^{2/3}$ (where α is the absorption coefficient, equal to $4\pi\lambda/k$, and E is the photon energy) were extrapolated to the photon energy axis. Other excitation models, such as indirect forbidden, indirect allowed, and direct allowed, were used but did not yield physically reasonable results. These models predict either near zero or negative onset energies for the B features. Near-zero values are inconsistent with the resistivity vs temperature curves, which indicate semiconducting rather than metallic behavior. In-plane transport properties of the annealed films were investigated using a Hall measurement system in the temperature range 100–310 K. Measurements were done in the van der Pauw geometry with square samples ($\sim 5 \times 5$ mm²) and silver paste in the corners.

Optical absorption spectra were calculated from first principles using a two-step procedure. First, structural parameters were determined using the periodic model approach and density functional theory (Fig. S1). We used a 40 atom ($2 \times 2 \times 2$) orthorhombic perovskite cell, La_{8-n}Sr_nFe₈O₂₄, where $8-n$ La and n Sr atoms were randomly distributed throughout the A sublattice. For simplicity, we considered only one configuration for each Sr concentration. The geometrical structures were optimized using PBEsol functional [31], as implemented in the Vienna Ab initio Simulation Package (VASP) [32]. The projector augmented-wave was used to approximate the electron-ion potential [33]; the $4 \times 4 \times 4$ Monkhorst-Pack k -grid was used for the Brillouin zone integration. The plane wave basis cutoff was set at 500 eV and the total energy was converged to 10^{-6} eV. Unless stated otherwise, all geometrical structures were fully relaxed.

In the second step, the pre-optimized LSFO solid solution lattices were modeled using an embedded cluster approach [34-36]; excitation energies and corresponding transition probabilities were calculated using TDDFT [37] as implemented in NWChem [38]. In the embedded cluster approach, a part of the lattice is treated quantum mechanically (referred to as the quantum cluster) and is embedded into the electrostatic and short-range potential generated by a surrounding lattice (referred to as the environment). To this end, we complemented the pre-optimized periodic model structures with auxiliary point charges, as described elsewhere [39,40], in order to eliminate all components of the low multipole moments from $m = 1$ (dipole) to $m = 4$ (hexadecapole) without affecting the charge neutrality condition. The modified LSFO supercells

were used to generate spherical nanoclusters (one for each periodic structure) of radius (R) equal to ~ 5.7 nm. The electrostatic potential in the central region of such clusters converges absolutely with increasing R . Its variations are less than 0.01 V within the quantum cluster for $R = 5.7$ nm (see Fig. S1 in the Supplementary Information section).

The quantum clusters were constructed so as to capture electronic structure changes associated with an increasing Sr concentration. In all cases, these clusters include eight Fe ions and all neighboring oxygen ions as well as seven A-site ions, these being either La^{3+} or Sr^{2+} (See Fig. S1). Cations adjacent to the quantum cluster are represented using effective core pseudopotentials that mimic the radius and ionic charges of Fe, Sr, and La. The details of the basis sets are described in the Supplemental Information. The ground state electronic structures of these clusters were calculated using B3LYP functional [41] in spin-polarized mode. Knowledge of the atomic orbital contributions to cluster orbitals and an ability to select occupied and virtual orbitals for the TDDFT active space allows us to assign contributions of various types of transitions to specific features in the experimental absorption spectra.

III. EXPERIMENTAL CHARACTERIZATION

A. Structure and Film Surface Quality

Figure 1(a) shows RHEED patterns for the as-grown LSFO films. These patterns exhibit sharp, unmodulated streaks, revealing excellent crystallinity and flat surfaces. Typical AFM images [Fig. 1(b)] for the as-grown LSFO films show clearly spaced surface steps, similar to those seen on the STO substrates. After oxygen plasma annealing to fully oxidize the films, X-ray reciprocal space maps (Fig. S2) of the film and substrate (103) peaks reveal that the LSFO films are fully strained to the substrate. The (002) peak of the annealed LSFO film systematically shifts to higher angle with increasing x , as shown in Fig. 1(c), indicating that the out-of-plane lattice parameter decreases (Table 1). Well-defined Kiessig fringes are visible in Fig. 1(b), confirming the high degree of crystallinity as well as thickness uniformity of these fully-strained films.

B. Core-level Photoemission Spectra

Figure 2(a) shows representative core-level spectra for the four elements in LSFO with various x values after removal from UHV to attach Au foils for binding energy calibration. The Fe $2p$ and O $1s$ line shapes change with x whereas those associated with Sr $3d$ and La $4d$ remain unchanged. The Fe $2p$ line shape change can be ascribed to a gradual increase in formal charge on Fe cations as holes are doped into the top of the VB, which in turn has substantial Fe $3d$ character, as discussed in conjunction with Fig. 3a. The O $1s$ line shape change is independent of the presence of slight amounts of surface contamination resulting from air exposure, but rather is correlated with hole doping of the VB (Fig. S3). A common shift to lower binding energy is measured for the O $1s$, Sr $3d$, and La $4d$ core levels due to the change in chemical potential with increasing x [28,42,43]. We average these three energy shifts to track this change. Figure 2(b) shows the chemical potential trend and indicates a monotonic downward shift with increasing hole concentration, similar to that seen in other hole-doped perovskite oxide alloys, such as $\text{La}_{1-x}\text{Sr}_x\text{TiO}_3$ [44], $\text{La}_{1-x}\text{Sr}_x\text{MnO}_3$ [45], and $\text{La}_{1-x}\text{Sr}_x\text{CrO}_3$ [42]. The overall trend in chemical potential nicely matches the trend in VB maximum (VBM) shown in Fig. S4 and Table 1, as well as the decrease in both the room-temperature resistivity [Fig. 2(c) and Fig. S5] and hopping activation energy [27]. The detailed rate of change of the chemical potential with x is different than that seen in ref. [28]. This difference is most likely related to inequivalent extents of oxidation in the two sets of LSFO films. Our post-annealing process is similar to that used in Ref. [27] and leads to complete oxidation. As a result, our $d\mu/dx$ behavior (Fig. 2b) nicely matches the trend in the hopping activation energy shown in Ref. [27]. Moreover, the R vs. T curves we present (Fig. S5) are very similar to those shown in Ref. [27].

The change in Fe valence with Sr doping is clearly seen in Fe $2p$ XPS and Fe K -edge NEXAFS spectra in Fig. 3. In order to more easily visualize the change in Fe $2p$ lineshape with x , we align all XPS spectra to place the corresponding O $1s$ peaks at 530.0 eV in order to remove the chemical potential change with x . The results are shown in Fig. 3(a). For pure LFO, the Fe $2p$ line shape is virtually identical to that in binary oxides containing Fe^{3+} , such as $\gamma\text{-Fe}_2\text{O}_3(001)$ [46]. However, the Fe $2p_{3/2}$, Fe $2p_{1/2}$ features become broader and shift to higher binding energy with increasing x , suggestive of progressive partial hole localization on B-site Fe cations. Moreover, the charge transfer satellites become weaker with increasing x and are not observed

for SFO ($x = 1$). The Fe $2p$ spectrum of SFO is very similar to that of Fe $2p$ in fully oxidized BaFeO₃ thin films [47], again consistent with hole doping on Fe sites, resulting in a formal charge larger than 3+. This trend is corroborated by the Fe K -edge NEXAFS data (Figure 3(b)). A systematic shift of the maximum absorption feature to higher x-ray energy with increasing x is clearly seen, again indicating an increase in formal charge. The increase in Fe valence should result in a decrease in the ionic radius, leading to an expected decrease in the (unconstrained) out-of-plane lattice parameter. This trend is clearly seen in the XRD results (see Fig. S2 and Table 1). Moreover, the small pre-edge feature in the Fe K -edge NEXAFS also increases with x , indicating an increase in hole concentration in the Fe $3d$ -derived VB, consistent with previous results [48]. Significantly, we did not observe a leveling off of either the absorption peak maximum energy shift or the intensity of the pre-edge feature as x approaches 1, as noted in earlier work [48]. We attribute this to a higher oxygen content in our films, particularly SFO.

The asymmetric broadening of the lattice O $1s$ peak at higher x values (Figs. 2a and S3) has not been previously observed and commented on in the literature. We suggest that this line shape change is due to hole delocalization over Fe and O sites driven by the considerable extent of Fe $3d - O 2p$ hybridization in the VB, as discussed in more detail below.

C. Electronic and Optical Properties

To gain deeper insight into the relationship between adding holes to VB and the optical properties of LSFO films, we correlate absorption data derived from SE with electronic densities of states. Figures 4(a) and 4(b) show absorption spectra for the LSFO film series plotted as raw data (a) and as Tauc plots (b) for direct, forbidden transitions (i.e. $(\alpha E)^{1/r}$ where $r = 3/2$). Characteristic features in the low-energy portion of the spectra are denoted as A and B. We show in Fig. 4(c) occupied and unoccupied densities of states taken from XPS VB and O K -edge NEXAFS, respectively. The energy scale for the NEXAFS spectra was aligned so the band gaps agree with those from the absorption spectra [Fig. 4(b)]. The spectra in Fig. 4(c) and their interpretations are qualitatively similar to those published previously by Wadati *et al.* [28], the principal difference being a weaker feature just above the Fermi level in our spectra. Our NEXAFS measurements were carried out using as-grown films in an ambient-pressure XPS chamber at the ALS at 300°C and 100 mTorr O₂. As a result, these films were probably not fully

oxidized, resulting in a lower intensity for this feature due to smaller hole concentrations that would be present in fully oxidized films.

To interpret the origin of features A and B, we also calculate the one-electron DOS and the absorption spectra for LSFO. Figure 4(e) shows the DOS obtained using an embedded cluster model and the B3LYP density functional. The distinct feature at the top of the VB in pure LFO [Fig. 4(c), $x = 0$] consists of hybridized O 2*p* and Fe 3*d* e_g orbitals, while unoccupied Fe 3*d* t_{2g} and e_g orbitals form the bottom of the conduction band (CB) [22,28]. Upon hole doping, the top of the VB becomes partially unoccupied and a new DOS feature appears above E_F (marked by an arrow in the $x = 0.2$ O *K*-edge NEXAFS spectrum in Fig. 4(c)), resulting in a narrowing of the gap. Previous reports [22,24,28] also assign the new feature above E_F to a split-off, empty Fe 3*d* e_g /O 2*p* hybridized band, consistent with our calculations. Therefore, we attribute feature B in the absorption spectra [Fig. 4(a)] to transitions from the top of the VB to the split-off empty Fe 3*d* e_g /O 2*p* hybridized band in the gap, as seen schematically in Fig. 4(d). The intensity of feature B increases and its energy drops with increasing x [Fig. 4(a)], consistent with the growth of the unoccupied DOS just above E_F and a closing of the gap due to hole doping.

In assigning feature A, we introduce the following notation based on LFO being a G-type antiferromagnet [49]. Each high-spin B-site Fe^{3+} ion with spin-up (\uparrow) 3*d* occupied (o) orbitals $e_g\uparrow o$ and $t_{2g}\uparrow o$, as well as virtual (v) spin-down (\downarrow) orbitals $e_g\downarrow v$ and $t_{2g}\downarrow v$, is adjacent to an Fe^{3+} ion with the opposite spin orientation ($e_g\downarrow o$, $t_{2g}\downarrow o$, $e_g\uparrow v$, and $t_{2g}\uparrow v$). Using these notations, we assign feature A to the spin-allowed transitions between neighboring sites Fe_1 and Fe_2 : O 2*p*/ Fe_1 $e_g\uparrow o \rightarrow Fe_2$ $t_{2g}\uparrow v$ and O 2*p*/ Fe_2 $e_g\downarrow o \rightarrow Fe_1$ $t_{2g}\downarrow v$, as shown schematically in Fig. 4(d). The A-type onset energies can be determined from Tauc plots, as seen in Fig. 4(b) and Table 1. Feature A becomes stronger and shifts to lower energy with increasing x . This shift reveals that the separation between the VB and the band derived from the virtual t_{2g} orbitals decreases with increasing x (Fig. S4). This trend is also apparent in our first-principles simulations. Fig. 4(e) shows the evolution of the virtual states with increasing x . As x increases, the separation between the occupied and virtual states decreases. Accordingly, the onset of transition A shifts to lower energy and excitations from deeper states in the O 2*p* band become possible, contributing to the intensity.

Theoretical spectra [Fig. 4(f)] were generated by calculating excitation energies and oscillator strengths for the 600 lowest-energy transitions that correspond to features A (green) and B (red). Each transition was represented using a Gaussian function with a full width at half maximum (FWHM) value of 0.1 eV. Oscillator strengths for optical transitions are sensitive to the details of the local environment, including lattice distortions due to alloy formation and vibrational amplitudes. In order to accurately account for these effects, we would need to average over all actual distributions of La and Sr atoms within the A sublattice, as well as over thermally induced atomic motion [15,35]. Here we account for thermal averaging in a more simple way by assigning the same oscillator strength to each transition, with only one La/Sr distribution in the A sublattice considered for each x value. The accuracy of this approximation can be evaluated by comparison of the calculated and measured absorption spectra for LFO. The low-energy peak at ~ 4 eV and the absorption increase at ~ 4.5 eV seen in Fig. 4(f) correspond to the experimentally observed features at 3.2 and 3.7 eV (Fig. 4(a)). Analysis of the molecular orbitals contributing to these transitions reveals that they originate from hybridized Fe e_g - o/O $2p \rightarrow t_{2g-v}$ excitations, as expected from the structure of the DOS, while the higher energy feature has an additional contribution due to excitations from pure O $2p$ orbitals located deeper in the VB to the t_{2g-v} orbitals. In agreement with the experimental data [Fig. 4(a)], our simulations also show that the optical absorption band A is visible in undoped LFO (Fig. 4(f), top panel) and its spectral weight changes: the onset of this band shifts to lower energy and its intensity increases with increasing x .

As mentioned above, the transfer of DOS from the top of the VB (occupied) to states just above E_F (unoccupied) that result from the formation of higher valent Fe creates new low-energy, intra-atomic optical transitions denoted as B in Fig. 4(a) and Fig. 4(d). The experimentally determined onset energy of this feature approaches zero with increasing x . This trend is consistent with the vanishing band gap in the periodic model simulations using the PBEsol density functional [Fig. S1(c)]. However, reproducing a vanishing band gap is problematic for the hybrid B3LYP functional due to the nature of its exchange-correlation term. As a result, our calculations do not reproduce the systematic shift of the onset of feature B with increasing x . That said, the electrostatic interaction between the excited electrons and holes shifts the onset of the optical absorption spectra in Fig. 4(f) to energies lower than the gap between the corresponding highest occupied and the lowest unoccupied one-electron energies in Fig. 4(e).

Importantly, the gradual increase in intensity of this feature is visible in both experimental and theoretical data. We note that transitions of the kind VB \rightarrow Fe e_g /O $2p$ transitions also contribute to feature A. While our data do not allow us to isolate these two contributions to feature A, we propose this could be achieved via mapping feature A as a function of strain, temperature and oxygen content.

IV. CONCLUSIONS

We show that Sr²⁺ substitution for La³⁺ in epitaxial La_{1-x}Sr_xFeO₃ thin films deposited on STO(001) increases the electrical conductivity as a result of hole doping of the VB, leading to a conversion from semiconducting to metallic behavior at x=1. The Fermi level drops toward the top of VB with increasing x. These changes in electronic structure are manifested by the formation of a new split-off band above the Fermi level seen in both experiment and first-principles calculations. The evolution of the low-energy optical absorption peaks can be explained by the changes in electronic structure in LSFO accompanying hole doping. Our calculations reveal that the top of the LFO VB consists of hybridized O $2p$ and Fe $3d e_g$ orbitals, whereas unoccupied Fe $3d t_{2g}$ and e_g orbitals form the bottom of CB. The optical absorption feature at $\sim 2.5 - 3$ eV is assigned to the spin-allowed transitions O $2p$ /Fe₁ $e_g \uparrow o \rightarrow$ Fe₂ $t_{2g} \uparrow v$ and O $2p$ /Fe₂ $e_g \downarrow o \rightarrow$ Fe₁ $t_{2g} \downarrow v$, where the e_g and t_{2g} orbitals are localized on adjacent ions Fe₁ and Fe₂. The new feature that forms just above the Fermi level is assigned to the split-off empty Fe $3d e_g$ /O $2p$ hybridized band resulting from hole doping. This feature gives rise to a new set of optical transitions from the VB at ~ 1 eV. The enhanced level of understanding of the electronic properties and optical transitions in LSFO presented here can facilitate the usefulness of LSFO in photocatalysis, photovoltaics, and electrocatalysis.

ACKNOWLEDGMENTS

This research was supported by the U.S. Department of Energy (DOE), Office of Basic Energy Sciences, Division of Materials Science and Engineering under award No. 10122. This research used resources of the Advanced Light Source, which is a DOE Office of Science User Facility under contract no. DE-AC02-05CH11231. O K -edge measurements and analysis were supported by the Linus Pauling Distinguished Post-doctoral Fellowship at Pacific Northwest National Laboratory (PNNL LDRD 69319). A portion of the work was performed at the W. R. Wiley Environmental Molecular Sciences Laboratory, a DOE User Facility sponsored by the Office of

Biological and Environmental Research. PNNL is a multi-program national laboratory operated for DOE by Battelle.

References

- [1] M. Imada, A. Fujimori, and Y. Tokura, *Rev. Mod. Phys.* **70**, 1039 (1998).
- [2] J. Coey, M. Viret, and S. Von Molnar, *Adv. Phys.* **48**, 167 (1999).
- [3] J. G. Bednorz and K. A. Müller, *Z. Phys. B Con. Mat.* **64**, 189 (1986).
- [4] J. Wang, J. Neaton, H. Zheng, V. Nagarajan, S. Ogale, B. Liu, D. Viehland, V. Vaithyanathan, D. Schlom, and U. Waghmare, *Science* **299**, 1719 (2003).
- [5] K. J. May, D. P. Fenning, T. Ming, W. T. Hong, D. Lee, K. A. Stoerzinger, M. D. Biegalski, A. M. Kolpak, and Y. Shao-Horn, *J. Phys. Chem. Lett.* **6**, 977 (2015).
- [6] J. Suntivich, K. J. May, H. A. Gasteiger, J. B. Goodenough, and Y. Shao-Horn, *Science* **334**, 1383 (2011).
- [7] J. Hwang, R. R. Rao, L. Giordano, Y. Katayama, Y. Yu, and Y. Shao-Horn, *Science* **358**, 751 (2017).
- [8] R. Nechache, C. Harnagea, S. Li, L. Cardenas, W. Huang, J. Chakrabartty, and F. Rosei, *Nat. Photonics* **9**, 61 (2015).
- [9] L. Wang, S. Dash, L. Chang, L. You, Y. Feng, X. He, K.-j. Jin, Y. Zhou, H. G. Ong, and P. Ren, *ACS Appl. Mater. Interfaces* **8**, 9769 (2016).
- [10] T. Ishihara, *Perovskite oxide for solid oxide fuel cells* (Springer Science & Business Media, 2009).
- [11] Y. Zhou, X. Guan, H. Zhou, K. Ramadoss, S. Adam, H. Liu, S. Lee, J. Shi, M. Tsuchiya, and D. D. Fong, *Nature* **534**, 231 (2016).
- [12] M. D. Scafetta, A. M. Cordi, J. M. Rondinelli, and S. J. May, *J. Phys. Condens. Matter* **26**, 505502 (2014).
- [13] S. Ishiwata, M. Tokunaga, Y. Kaneko, D. Okuyama, Y. Tokunaga, S. Wakimoto, K. Kakurai, T. Arima, Y. Taguchi, and Y. Tokura, *Phys. Rev. B* **84**, 054427 (2011).
- [14] K. Nakamura, H. Mashiko, K. Yoshimatsu, and A. Ohtomo, *Appl. Phys. Lett.* **108**, 211605 (2016).
- [15] P. Tang, Y. Tong, H. Chen, F. Cao, and G. Pan, *Curr. Appl. Phys.* **13**, 340 (2013).
- [16] M. Nakamura, F. Kagawa, T. Tanigaki, H. Park, T. Matsuda, D. Shindo, Y. Tokura, and M. Kawasaki, *Phys. Rev. Lett.* **116**, 156801 (2016).
- [17] A. Fossdal, M. Menon, I. Wærnhus, K. Wiik, M. A. Einarsrud, and T. Grande, *J. Am. Ceram. Soc.* **87**, 1952 (2004).
- [18] O. Clemens, M. Kuhn, and R. Haberkorn, *J. Solid State Chem.* **184**, 2870 (2011).
- [19] L. Wang, Y. Du, L. Chang, K.A. Stoerzinger, M.E. Bowden, J. Wang, and S.A. Chambers, *Appl. Phys. Lett.* **112**, 261601 (2018).
- [20] S. She, J. Yu, W. Tang, Y. Zhu, Y. Chen, J. Sunarso, W. Zhou, and Z. Shao, *ACS Appl. Mater. Interfaces* **10**, 11715 (2018).
- [21] K. A. Stoerzinger, L. Wang, Y. Ye, M.E. Bowden, E. J. Crumlin, Y. Du, and S. A. Chambers, *J. Mat. Chem. A* **6**, 22170 (2018).
- [22] M. Abbate, F.M.F. De Groot, J.C. Fuggle, A. Fujimori, O. Strebel, F. Lopez, M. Domke, G. Kaindl, G.A. Sawatzky, and M. Takano, Y. Takeda, H. Eisaki, S. Uchida, *Phys. Rev. B* **46**, 4511 (1992).

- [23] H. Wadati, A. Chikamatsu, M. Takizawa, R. Hashimoto, H. Kumigashira, T. Yoshida, T. Mizokawa, A. Fujimori, M. Oshima, and M. Lippmaa, M. Kawasaki, H. Koinuma, *Phys. Rev. B* **74**, 115114 (2006).
- [24] S. Y. Smolin, M. D. Scafetta, A. K. Choquette, M. Y. Sfeir, J. B. Baxter, and S. J. May, *Chem. Mat.* **28**, 97 (2015).
- [25] A. M. Ritzmann, A. B. Muñoz-García, M. Pavone, J. A. Keith, and E. A. Carter, *Chem. Mat.* **25** 3011 (2013).
- [26] Y. Xie, M. D. Scafetta, R. J. Sichel-Tissot, E. J. Moon, R. C. Devlin, H. Wu, A. L. Krick, and S. J. May, *Adv. Mat.* **26**, 1434 (2014).
- [27] Y. Xie, M. Scafetta, E. Moon, A. Krick, R. Sichel-Tissot, and S. May, *Appl. Phys. Lett.* **105**, 062110 (2014).
- [28] H. Wadati, D. Kobayashi, H. Kumigashira, K. Okazaki, T. Mizokawa, A. Fujimori, K. Horiba, M. Oshima, N. Hamada, and M. Lippmaa, M. Kawasaki, H. Koinuma, *Phys. Rev. B* **71**, 035108 (2005).
- [29] M. D. Scafetta, Y. Xie, M. Torres, J. Spanier, and S. May, *Appl. Phys. Lett.* **102**, 081904 (2013).
- [30] P. C. Rogge, R. U. Chandrasena, A. Cammarata, R. J. Green, P. Shafer, B. M. Lefler, A. Huon, A. Arab, E. Arenholz, and H. N. Lee, *Phys. Rev. Mat.* **2**, 015002 (2018).
- [31] J. P. Perdew, A. Ruzsinszky, G. I. Csonka, O. A. Vydrov, G. E. Scuseria, L. A. Constantin, X. Zhou, and K. Burke, *Phys. Rev. Lett.* **100**, 136406 (2008).
- [32] G. Kresse and D. Joubert, *Phys. Rev. B* **59**, 1758 (1999).
- [33] P. E. Blöchl, *Phys. Rev. B* **50**, 17953 (1994).
- [34] Y. Wang, K. Lopata, S. A. Chambers, N. Govind, and P. V. Sushko, *J. Phys. Chem. C* **117**, 25504 (2013).
- [35] P. V. Sushko, L. Qiao, M. Bowden, T. Varga, G. J. Exarhos, F. K. Urban III, D. Barton, and S. A. Chambers, *Phys. Rev. Lett.* **110**, 077401 (2013).
- [36] I. H. Nayyar, S. E. Chamberlin, T. C. Kaspar, N. Govind, S. A. Chambers, and P. V. Sushko, *Phys. Chem. Chem. Phys.* **19**, 1097 (2017).
- [37] S. Hirata and M. Head-Gordon, *Chem. Phys. Lett.* **314**, 291 (1999).
- [38] M. Valiev, E. J. Bylaska, N. Govind, K. Kowalski, T. P. Straatsma, H. J. Van Dam, D. Wang, J. Nieplocha, E. Apra, and T. L. Windus, *Comp. Phys. Commun.* **181**, 1477 (2010).
- [39] P. V. Sushko and I. V. Abarenkov, *J. Chem. Theory Comput.* **6**, 1323 (2010).
- [40] I.V. Abarenkov, *Phys. Rev. B* **76**, 165127 (2007).
- [41] A. D. Becke, *J. Chem. Phys.* **98**, 1372 (1993).
- [42] K. H. L. Zhang, Y. Du, P.V. Sushko, M. E. Bowden, V. Shutthanandan, S. Sallis, L. F. Piper, and S. A. Chambers, *Phys. Rev. B* **91**, 155129 (2015).
- [43] A. Sawa, A. Yamamoto, H. Yamada, T. Fujii, M. Kawasaki, J. Matsuno, and Y. Tokura, *Appl. Phys. Lett.* **90**, 252102 (2007).
- [44] A. Fujimori, A. Ino, J. Matsuno, T. Yoshida, K. Tanaka, and T. Mizokawa, *J. Electron. Spectros. Relat. Phenomena* **124**, 127 (2002).
- [45] K. Horiba, A. Chikamatsu, H. Kumigashira, M. Oshima, N. Nakagawa, M. Lippmaa, K. Ono, M. Kawasaki, and H. Koinuma, *Phys. Rev. B* **71**, 155420 (2005).
- [46] S.A. Chambers and S. Joyce, *Surf. Sci.* **420**, 111 (1999).
- [47] S. Chakraverty, T. Matsuda, N. Ogawa, H. Wadati, E. Ikenaga, M. Kawasaki, Y. Tokura, and H. Hwang, *Appl. Phys. Lett.* **103**, 142416 (2013).

- [48] C. Chang, G. Chern, M. Tai, Y. Su, C. Dong, S. Liu, C. Hwang, and P. Tseng, *Jpn. J. Appl. Phys.* **38**, 108 (1999).
- [49] J. E. Kleibecker, Z. Zhong, H. Nishikawa, J. Gabel, A. Müller, F. Pfaff, M. Sing, K. Held, R. Claessen, G. Koster, and G. Rijnders, *Phys. Rev. Lett.* **113**, 237402 (2014).

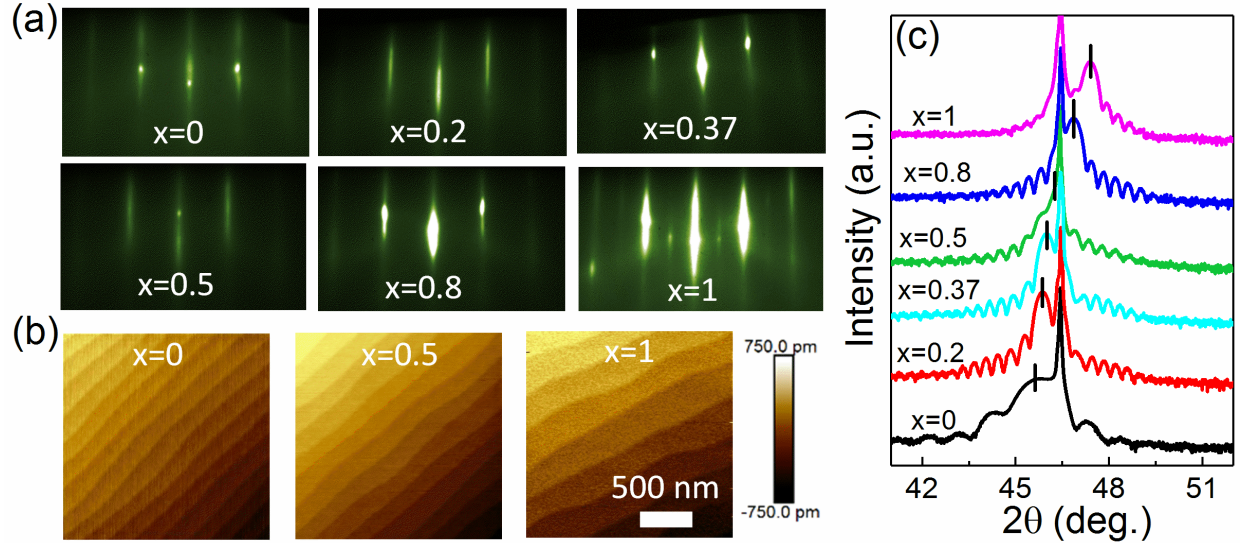


FIG. 1. (a) RHEED patterns for the as-grown $\text{La}_{1-x}\text{Sr}_x\text{FeO}_3$ films on $\text{STO}(001)$ viewed along the $[100]$ zone axis. (b) Representative AFM images for the as-grown LSFO films with $x = 0, 0.5$ and 1 on $\text{STO}(001)$. The scan image size is $2 \mu\text{m} \times 2 \mu\text{m}$. (c) XRD θ - 2θ scans of oxygen plasma annealed films near the (002) peak for the LSFO/ $\text{STO}(001)$ film set.

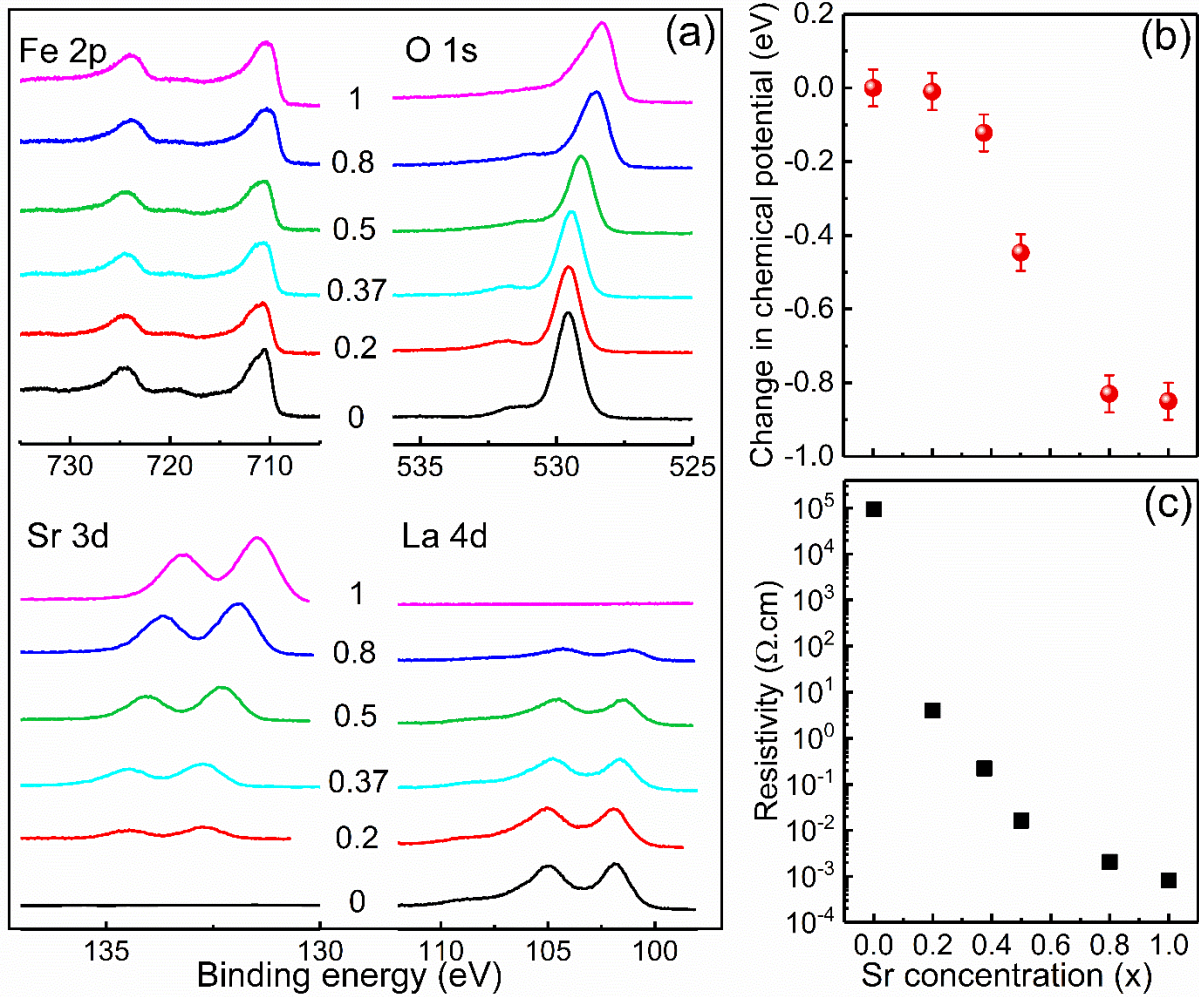


FIG. 2. (a) Fe 2*p*, O 1*s*, Sr 3*d* and La 4*d* XPS spectra for La_{1-x}Sr_xFeO₃ with various *x* values. The binding energy scales were calibrated using the Au 4*f*_{7/2} peak binding energy (84.00 eV). (b) Average chemical potential shift deduced from O 1*s*, Sr 3*d* and La 4*d* binding energies. (c) Room temperature resistivity vs *x*.

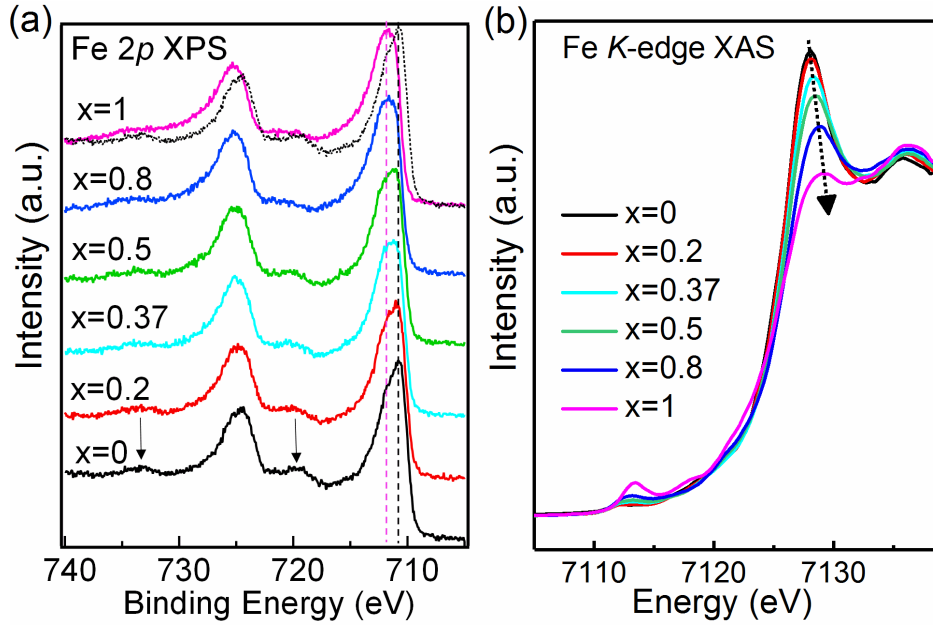


FIG. 3. (a) Fe $2p$ core level XPS spectra for $\text{La}_{1-x}\text{Sr}_x\text{FeO}_3$ with various x values. All spectra are shifted so the associated O $1s$ peaks fall at 530.0 eV. As a guide to the eye, we mark the core-level peaks of the LFO (black) and SFO (magenta) films with dashed lines. For comparison with $x = 1$, we replot the Fe $2p$ spectrum of LFO ($x=0$) as a dotted line. The satellite peaks for Fe^{3+} (indicated by arrows) are absent in SrFeO_3 (Fe^{4+}). (b) Fe K -edge NEXAFS for $\text{La}_{1-x}\text{Sr}_x\text{FeO}_3$ with various x values. The dashed arrow indicates the peak shift.

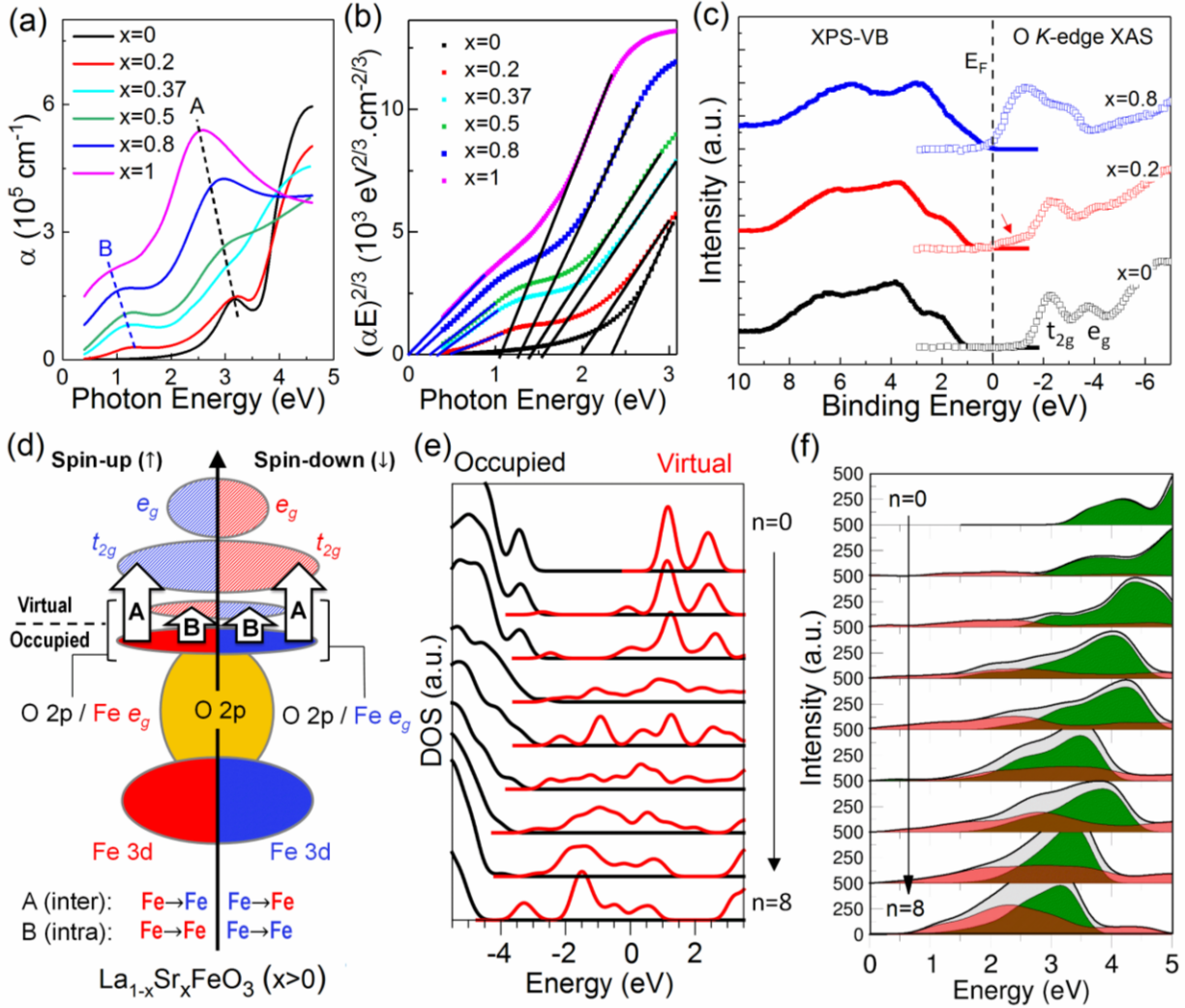


FIG. 4. (a) Absorption spectra for $\text{La}_{1-x}\text{Sr}_x\text{FeO}_3$ films deposited on $\text{STO}(001)$. (b) Tauc plots of $(\alpha E)^{2/3}$ versus photon energy E for the direct dipole-forbidden excitations. The resulting onsets of transitions A and B, shown as extrapolations to the energy axis, are summarized in Table 1. (c) XPS-VB (left, filled symbols) and O K-edge XAS (right, open symbols) for selected LSFO films. (d) Schematic of the electronic structure and optical transitions for $\text{La}_{1-x}\text{Sr}_x\text{FeO}_3$ ($x > 0$). Red and blue colors refer to neighboring Fe atoms (labeled as Fe_1 and Fe_2 in the text) that carry ground-state spin-density up (\uparrow) and down (\downarrow), respectively. Solid and dashed areas correspond to the occupied and virtual one-electron states. Hybridization of O 2p and Fe 3d e_g forms a distinct feature at the top of the valence band, which becomes partially depopulated for $x > 0$. Transitions A (inter-atomic) and B (intra-atomic) as indicated with arrows. (e) $\text{La}_{8-n}\text{Sr}_n\text{Fe}_8\text{O}_{24}$ one-electron DOS calculated using B3LYP with an embedded cluster. Here, the highest occupied (black) and the lowest unoccupied (red) one-electron states are separated by a few tenths of an eV for $n > 0$. A small overlap between the tails of the occupied and unoccupied DOS (where it exists) is a result

of Gaussian broadening, rather than a metallic electronic structure. (f) Low-energy region of the optical absorption spectra calculated using TDDFT and B3LYP; green, red, and grey colors indicate contributions due to A- and B-type transitions, and their sum, respectively.

Table 1. LSFO film thickness (estimated from RHEED oscillations), calculated x value (see Supporting Information), c-axis lattice parameter [Fig. 1(c)], onset of optical transitions A and B [Fig. 4(a)], and the valence band maximum (Fig. S3).

Composition	Thickness (nm)	Calculated x value	c-axis lattice parameter (Å)	Onset of Transition A (eV)	Onset of Transition B (eV)	VBM (eV)
x = 0	10	..	3.974	2.30(4)	..	1.02
x = 0.2	30	0.21	3.955	1.97(4)	0.49(4)	0.84
x = 0.37	30	0.35	3.943	1.53(4)	0.34(4)	0.70
x = 0.5	30	0.53	3.915	1.40(4)	0.23(4)	0.49
x = 0.8	30	0.77	3.871	1.26(4)	0.10(4)	0.17
x = 1	30	..	3.831	1.05(4)	0	0